Effects of scanning path gradient on the residual stress distribution and fatigue life of AA2024-T351 aluminium alloy induced by LSP

Enoch Asuako Larson, Xudong Ren, Samuel Adu-Gyamfi, Hongfeng Zhang, Yunpen Ren

PII: S2211-3797(18)33165-6
DOI: https://doi.org/10.1016/j.rinp.2019.02.059
Reference: RINP 2123

To appear in: *Results in Physics*

Received Date: 26 November 2018
Revised Date: 17 February 2019
Accepted Date: 17 February 2019

Please cite this article as: Asuako Larson, E., Ren, X., Adu-Gyamfi, S., Zhang, H., Ren, Y., Effects of scanning path gradient on the residual stress distribution and fatigue life of AA2024-T351 aluminium alloy induced by LSP, *Results in Physics* (2019), doi: https://doi.org/10.1016/j.rinp.2019.02.059

Effects of scanning path gradient on the residual stress distribution and fatigue life of AA2024-T351 aluminium alloy induced by LSP

Enoch Asuako Larson, Xudong Ren*, Samuel Adu-Gyamfi, Hongfeng Zhang, Yunpen Ren

School of Mechanical Engineering, Jiangsu University, Zhenjiang, 212013, PR China

Abstract

Laser shock peening (LSP) is a superficial treatment process employed to induce beneficial residual stress to retard fatigue crack growth, resist corrosion and wear and enhance the mechanical properties of metals. This research study the effects of scanning path gradient on the residual stress and fatigue life of AA2024-T351 aluminum alloy induced by LSP using experiment and 3D FE simulation to optimize the scanning path gradient. The material under study is of great importance in the aerospace industry on fuselage and lugs. Two divergent strategies were used, the scanning path gradient (strategy 1) and the scanning path in advancing direction (strategy 2) both on double-sided dog-bone specimen, and their residual stresses and fatigue life was compared. After LSP, both the LSP treated specimens residual stress and fatigue life were improved. The results showed that the fatigue life of the scanning path gradient was improved by 69.3% while that of the scanning path in advancing direction was improved by 93.5%. In addition, the magnitude of the residual stress on the apex surface was observed to be higher than the bottom surface. Results of the scanning path gradient for the residual stress was calculated by the 3D FE method and it was found to be in good agreement with the experiment results. We observed the presence of tensile residual stresses in between the apex and bottom surfaces after LSP.

Keywords: Laser shock peening (LSP), residual stress, fatigue life, scanning path gradient.

* Corresponding author. E-mail address: renxd@mail.ujs.edu.cn (Ren Xudong).

1. Introduction

Mechanical surface improvement treatment including ultrasonic shot peening, and shot peening(SP) are usually applied to extend the fatigue life [1], enhance the mechanical property, corrosion [2] and wear [3] resistant of metals. However, LSP is considered a novel surface treatment method peened on metal materials to improve the fatigue life by inducing beneficial compressive residual stresses (CRS) exceeding up to 1 mm underneath the apex surface which is depended on the type of material and the energy density [4]–[7] employed. Fig.1 illustrates a simple LSP setup used in this experiment. Several authors have stated that residual stress induced by LSP generate higher magnitude and greater in-depth compared to shot peening (SP), thus implying that fatigue life extension by laser peening treatment is of high superior quality than the ones produced by SP [8], [9]. LSP to a great extent is utilized to extend the fatigue life of several materials like aluminium alloys [10], stainless steel [11], [12], titanium alloys [13] and nickel-based super alloy [14] in several aerodynamic components. In addition, the application of 2D [4], [14], [15] and 3D [5], [16]–[18] FE simulation was created to predict residual stress and fatigue life in both single and multiple peening impacts and on single and double-sided specimens. Peyre et al. [19] studied the impact of process parameters induced by LSP on residual stress fields putting together strain rate dependent, mechanical behaviour and shockwave hydrodynamics by FEM simulation. Amarchinta et al. [20] studied the material model validation for LSP process simulation. Their study reported that the Johnson-Cook material model induced by LSP produced better residual stress distribution. Su et al. [21] examined the influence of LSP assisted via dynamic strain aging on tensile fatigue life of aluminum alloy welded joints. They stated that, laser peening assisted via dynamic strain aging increased the fatigue life of the aluminum alloy specimen to about 1.4 times than that of the strengthened joints [21]. Peyre et al. [22] reported that LSP can extend the fatigue life and in addition, impede against stress corrosion cracking

(SCC) on metallic materials. Various published literatures have also indicated that laser peening parameters like laser wavelength, laser pulse duration, laser spot diameter, laser energy per pulse and number of successive peening have significant influence on the induced residual stress on several metallic alloys [23]–[25]. Research investigation by different authors have stated that the induced residual stress by LSP is influenced by the pulse sequence and the specimen geometry [17], [26]. Samuel et al. [27] studied the effect of LSP scanning patterns on residual stress distribution and fatigue life of AA2024 aluminum alloy. They reported that the FE simulation results demonstrated that the residual stress distribution was influenced by the LSP scanning patterns. Kan Ding and Lin Ye [28] studied FE simulation on multiple LSP of 35CD4 steel alloy. They stated that the residual stress can be improved deeper beneath the surface by multiple LSP impacts at the same point. However, very few research investigations have been carried out on the effect of scanning path gradient on residual stress and fatigue life by LSP. Gariépy et al. [29] studied the microstructural state of AA2024 with T351 that was shot peened and examined by the EBSD analysis. They reported of an unindexable structure at the near surface with great dislocation densities and enormously small dislocation substructures. Hombergsmeier et al. [30] investigated on fatigue crack retardation in LSP and SP treated of AA2024-T3 aluminium specimen outside the initial notch. The effect of LSP on the retardation of FCP rate was as a result of the induced high residual stresses, which was generated in the 2 mm thick sheet.

The object of this paper is to examine the effect of scanning path gradient on residual stress distribution and fatigue life of AA2024-T351 aluminium alloy subjected with LSP. Two different scanning path strategies were investigated by the 3D FE method and experiment method to evaluate the residual stress distribution and fatigue life. Discussions on each of the scanning strategy is analysed based on the residual stress and the fatigue test results. The 3D FE simulation was used to predict the residual stress subjected by LSP on

double-sided specimen. We further investigated the correlation between the LSP scanning strategies and the residual distribution in the laser affected region. We also determined and compared the fatigue life of both the LSP treated and untreated specimens. Finally, the fracture surfaces of the specimens were analysed sequentially.

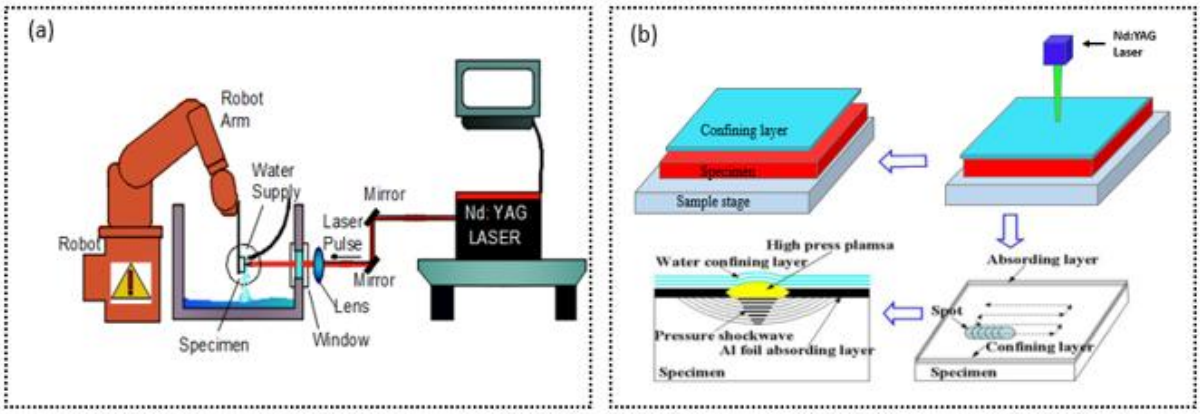

Fig. 1 (a) Experimental setup of LSP process (b) Magnified of specimen setup.

2. Experimental details

2.1 Materials and methods

The AA2024-T351 aluminium alloy material was wire cut into the shape of the dog-bone specimen with 3 mm thickness as shown in Fig. 2. The chemical composition and mechanical properties of the specimen is displayed in Table 1 and Table 2, respectively. Prior to LSP, the specimens were ground with silicon carbide (SiC) paper to the grade #1000 and then cleaned in alcohol. The laser shock peening was performed on a Q-switched Neodymium-doped Yttrium Aluminum Garnet (Nd:YAG) laser system operated over 1064 nm wavelength and 10 ns pulse width. The laser spot diameter was 3 mm. The pulse energy employed in this experiment was 3.5 J. Further detail parameters of the LSP experiment is presented in Table 3. The LSP specimen was held in the fixture and is manipulated by an automated robot with both ends clamped to achieve the desired pulse sequence of the fixed laser beam.

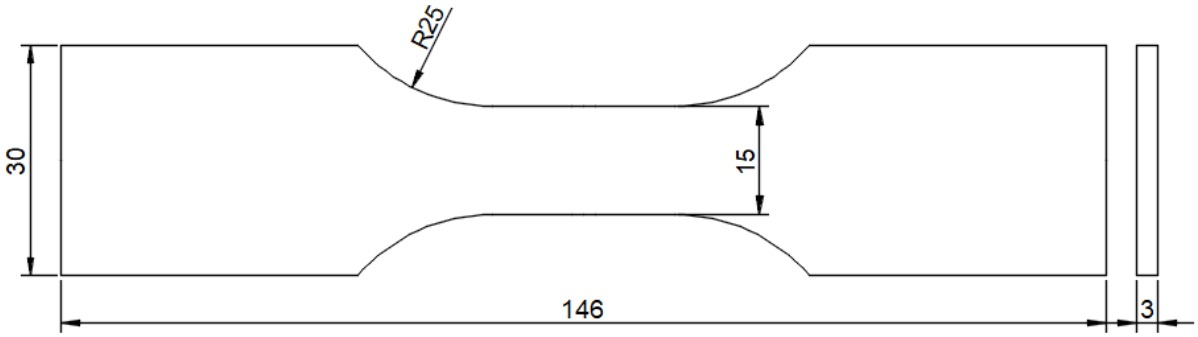

Fig. 2. Dimensions of fatigue specimens.

Table 1 Chemical composition of AA2024-T351 aluminium alloy (wt. %).

Cu	Mg	Mn	Si	Fe	Zn	Cr	Ti	Al
4.9-4.9	1.2-1.8	0.3-0.9	0.5	0.5	0.25	0.1	0.15	Bal.

Table 2 Mechanical properties of Al 2024-T351 aluminium alloy.

Material	Tensile strength (MPa)	Yield strength (MPa)	Elongation at fracture (%)	Elasticity modulus (GPa)	Poisson ratio
Al 2024-T351	421.8	369.0	19.6	72.4	0.33

Table 3 LSP processing parameters.

Processing parameters	Pulse energy (J)	Spot diameter (mm)	Pulse width (ns)	Overlapping rate (%)	Laser wavelength (nm)
Value	3.5	3	10	50	1064

2.2 Fatigue test

The fatigue experiment was performed on the SDS 100 fatigue machine with a load capacity ranging between –50 kN ~ +50 kN (Changchun Research Institute for Mechanical Science Co., Ltd., China). The machine was operated to perform fatigue test for both LSP treated at the different scanning path strategy and untreated specimen. In all, fifteen specimens were employed for the fatigue test. All the fatigue experiment was operated at

room temperature. The fatigue experiment frequency used was 10 Hz with a load ratio of R = 0.1. A maximum stress in the fatigue cycle of 200 MPa was performed on both the untreated and the LSP treated specimens.

2.3 Residual stress measurement

Residual stress measurement of the LSP treated and untreated specimens was determined by the X-ray diffraction (XRD) with $Sin^2\Psi$ method. The values for Ψ was set at 0.0^o, 25.0^o, 35.0^o and 45.0^o, respectively. The current and X light tube voltage was 6.0 mA and 22.0 kV, respectively with 0.50 s counting time. The X-ray beam diameter used was 1 mm. The diffraction plane was α phase (311) plane and an X-ray source of Cu-Kα ray. The feed angle of the ladder scanning and stress constant K, was 0.2^o/s and -166 MPa/(^{o}), respectively. The scanning starting angle and ending angle was 130^o and 143^o, respectively. The specimen layer was removed with the electro-polishing to achieve the depth profiles of the compressive residual stress and to avoid the influence of external stress induced by peening of the material on the compressive residual stress. Electro-polishing was performed in a solution of 3.5% saturated sodium chloride solution, and the material removal rate was carefully controlled by an applied voltage and time. The untreated area surrounding the LSP treated region was masked to provide uniformity and coherence during the material removal rate.

2.4 Finite element modelling (FEM)

The commercial FEM ABAQUS 6.13 software was employed in the LSP simulation process in this work. FEM based 3D model was developed and used to analyse the distribution and stress/strain after laser peening [31]. The FEM utilized in this simulation comprise of eight-node bricks (C3D8R) with reduced integration and hourglass control in the LSP shocked region generating a denser mesh. The geometry of the model employed in the FEM simulation is the same as the experimental. 125,850 linear hexahedron elements were used. The specimen target area was 30 × 15 mm and the element size of the LSP region was 100 × 100 × 30 μm. During the FEM simulation, the symmetrical ends of the 3D model was constrained for the static calculation of the residual stress. Fig. 3 is an illustration of the 3D model and mesh employed in the FEM simulation. Throughout the LSP process, the metallic

material experienced high strain rates beyond 10^6 s^{-1} at a limited time [32]. The elastic-plastic performance was of the Aluminum alloy specimen was simulated by the mechanical properties and the acoustic impedance that incorporates strain rate dependence that is taken into account by the Johnson-Cook material model [17]. The Johnson-Cook (J-C) strain rate sensitivity plastic constitutive model was used to simulate accurately the dynamic response in the high strain rate between 10^2 and 10^6 s^{-1} for the laser peened specimens.

$$\sigma = (A + B\varepsilon^n)\left[1 + C\ 1n\left(\frac{\varepsilon'}{\varepsilon_0'}\right)\right]\left[1 - \left(\frac{T-T_0}{T_m-T_0}\right)^m\right] \quad (1)$$

where ε is the effective plastic strain, ε' is the effective plastic strain rate and ε_0'=1.0 s^{-1}. T_0 and T_m are the room temperature and melting temperature, respectively. The experimentally determined constants are *A*, *B*, C, and *n*. where A is the yield stress, B is the work hardening modulus, *n* is the work hardening co-efficient and C is the strain rate sensitivity. In this work, the thermal term of the J-C equation is not considered because, the LSP is a thermal isolation process. The J-C material constitutive model for AA2024-T351 aluminum alloy is given in Table 4.

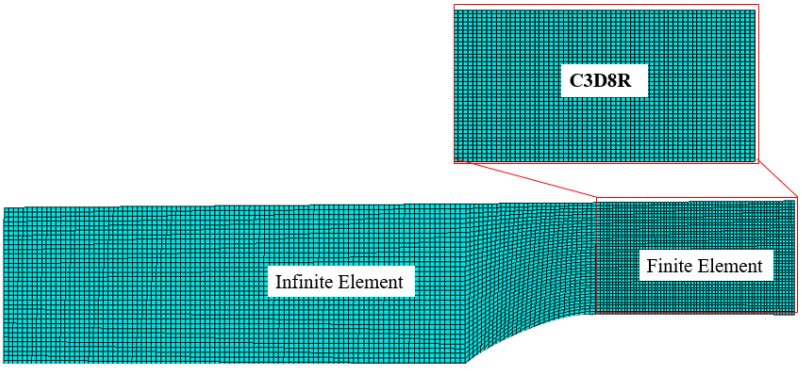

Fig. 3 (a) The 3D FEA model (b) view of FE area.

Table 4 Johnson-Cook material constant for AA2024-T351 aluminum alloy.

A (MPa)	*B* (MPa)	*n*	C	*m*	$\dot{\varepsilon}_0$
369	684	0.73	0.0083	1.70	1

During the LSP process, the shock-waves propagates from the apex surface into the metallic material, thus, there is the occurrence of plastic deformation until the point where the peak stress is far greater than the Hugoniot elastic limit (HEL) of the metallic material. This induces compressive residual stresses across the laser affected depth [33]. The mathematical expression for HEL is related to the Poisson ratio and dynamic yield strength, σ_{dy} according to [4], [7], [9], [28], [34]–[35] is given as;

$$HEL = \frac{1-v}{1-2v}\sigma_{dy} \tag{2}$$

where, v is the Poisson ratio, σ_{dy} is the dynamic yield strength at high strain rate. Fabbro et al. [37] suggested that plastic deformation continues until such a time that the peak dynamic stress declined beneath the dynamic yield strength of the metallic material. Ballard et al. [38] reported that the induced laser can lead to plastic deformation is a linear dependent on the ratio of the peak pressure to the Hugoniot elastic limit. The mathematical equation for the maximum peak pressure induced by the plasma, P_{max}, is given according to [4], [7], [9], [28], [35],

$$P_{max}\ (GPa) = 0.01\sqrt{\frac{\alpha}{2\alpha+3}}\sqrt{Z(gcm^{-2}s^{-1})}\ \sqrt{I_0(GWcm^{-2})} \tag{3}$$

where I_o is the laser power density, α is the efficiency of the interaction and Z is the reduced shock impedance between the material and the confining medium. In this case, the model is regarded as a perfect gas and the impedance between the metallic material and the confine layer [7], [36], is expressed as;

$$Z = 2\ /\ \left(\frac{1}{Z_1} + \frac{1}{Z_2}\right) \tag{4}$$

$$I_o = \frac{4E}{\pi d^2 t_p} \quad (5)$$

where Z_1 and Z_2 are the shock impedances for the coating aluminium foil (1.420 × 10^6 g/cm^{-2}.s^{-1}) and the confinement median, water (0.165 × 10^6 g/cm^{-2}.s^{-1}), respectively. E is the laser pulse energy (J). t_p is the pulse time (ns). d is the diameter of the laser pulse. The pressure evolution of the laser induced shockwave is shown in Fig. 4.

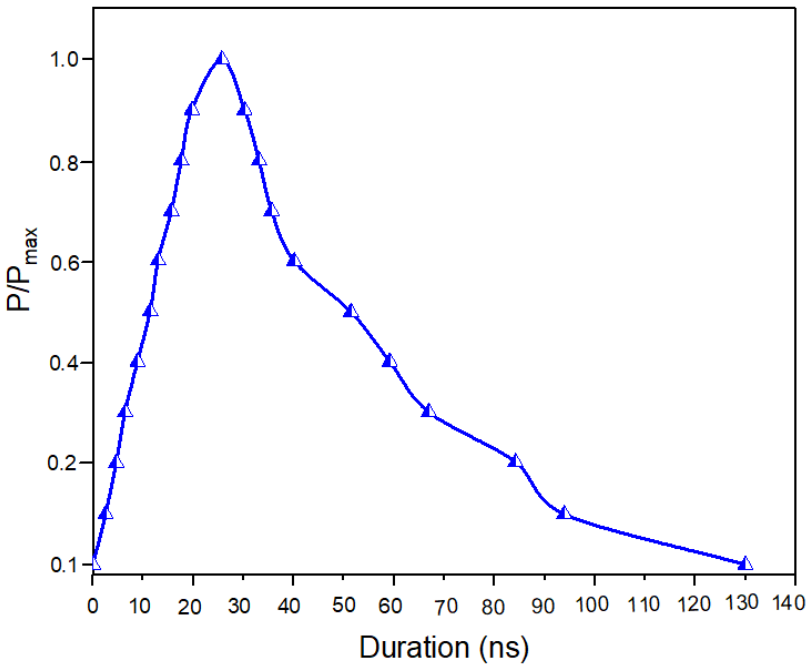

Fig. 4 Pressure evolution shock of laser induced shockwave.

2.5 Scanning strategies and residual stress distribution

2.5.1 Strategy 1: Scanning path gradient

The laser pulse sequence was applied by the scanning path gradient (strategy 1) on both the apex and bottom surfaces of the specimen as shown in Fig. 5(a). In all a total of 798 laser pulses was used in strategy 1. Laser pulses of 342, consisting of firing a first layer of scanning path on the shocked area 30 × 15 mm at the LSP treated zone. The second layer of scanning path gradient was laser peened with four paths at the front edge and four paths at the back-edge area with 304 laser pulses. The third layer scanning path gradient was laser peened

with two paths at the front edge and two paths at the back-edge area with 152 pulses. Fig. 5(a) displays the FE simulation results after employing strategy 1. During the LSP treatment, the apex surface was initially laser peened first followed by the bottom surface, thus resulting in differences in residual stress on the superficial layer on both surfaces.

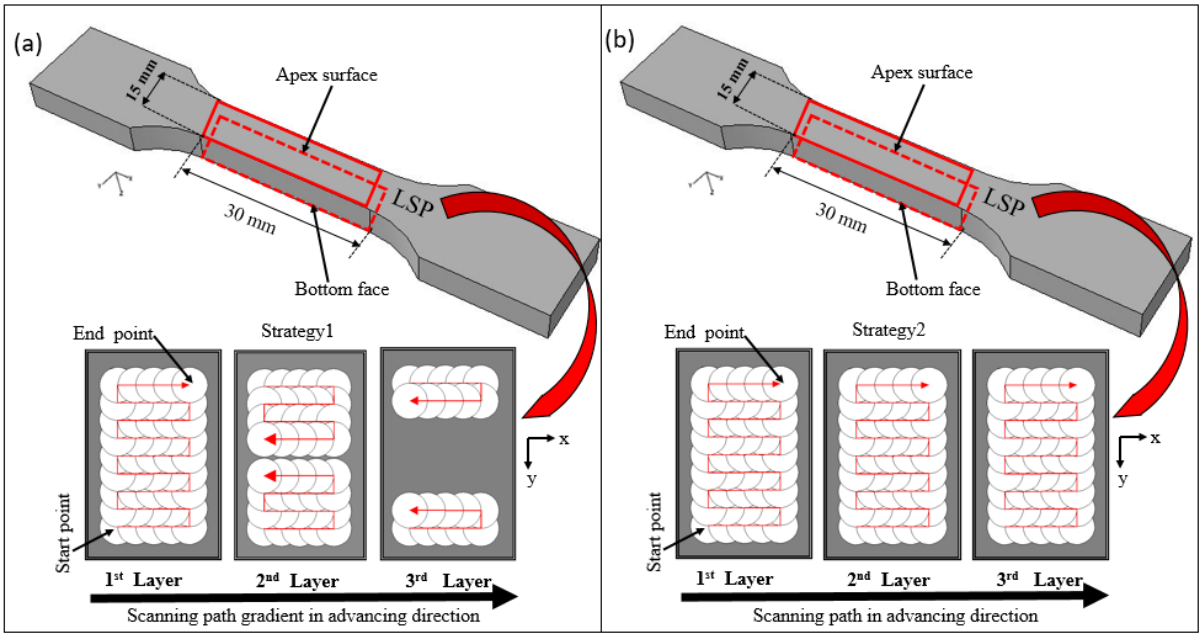

Fig. 5 Scanning path pattern employed in layers (a) Strategy 1 and (b) Strategy 2.

2.5.2 Strategy 2: Scanning path in advancing direction

The second laser pulse sequence is the scanning path in advancing direction (strategy 2) as shown earlier in Fig. 5(b). In all, 1,026 laser pulses were used in strategy 2. In this strategy, a first layer of laser pulses 342 was shot along the x-axis (fatigue applied load) in sequence on the shocked area 30 × 15 mm in a zig-zag scanning fashion. The second layer was shot on the target area just like the first layer from the start point to the end point with 342 laser pulses. Then, the third layer was also shot on the target area in sequence with 342 laser pulses from the start to the end point. The FE simulation results is shown in Fig. 5(b) after strategy 2. The view from the 3D surface can be visualized with residual stresses and induced tensile stresses at the middle section of the specimen.

3. Results and discussion

3.1 FEM simulation and residual stress distribution

In all, a total of 1,824 laser pulses were shot on the specimen target area used by the two divergent strategy. To reduce the simulation processing time in the shortest possible, the dog-bone specimen was reduced to one quarter and simulated to analyse the stress shown in Fig. 3. The symmetrical sides were boundary condition. The residual stress was analysed in ten different locations within the LSP processing area for all the specimens. The residual stress was measured along the x-axis (S11/σ_{xx}), which is along the fatigue applied load. Results of the residual stresses were compared between the experimental and FE simulation and they showed good agreement (see Fig. 6). The location on the points along A-B_1, A-B, C-D, and E-F are specified on the LSP treated specimen cross-section as shown in Fig. 7(a) and (b) as the path for the stress measurement. They are defined to link the specimen thickness from the apex to the bottom surfaces. The points A-B_1 is the mid location of the points from the apex surface to 0.5 mm depth along the path of the specimen. Points A, C and E are the edges of the apex surface and are connected to the points B, D and F of the edges on the bottom surface. After laser peening, we observed the presence of tensile residual stresses found in between the compressive residual stresses at both the apex and bottom surfaces[6]. The FE simulation results in Fig. 7(a) and (b) show variations in the compressive residual stress in depth with noticeable differences of residual stresses at the apex and bottom surfaces. The simulation results revealed that the magnitude of the induced residual stresses was not symmetrical in depth, so the apex surface was more compressive than the bottom surface because both surfaces were not concurrently laser peened (Figs. 9, 10 & 11). The induced residual stresses on the superficial layer in strategy 2 is similar to strategy 1 at the points A-B. The middle section tensile stresses in strategy 1 was less tensile than in strategy

2. Fig. 8 indicates the 2D simulation results after each scanning layer for Strategy 1 and Strategy 2.

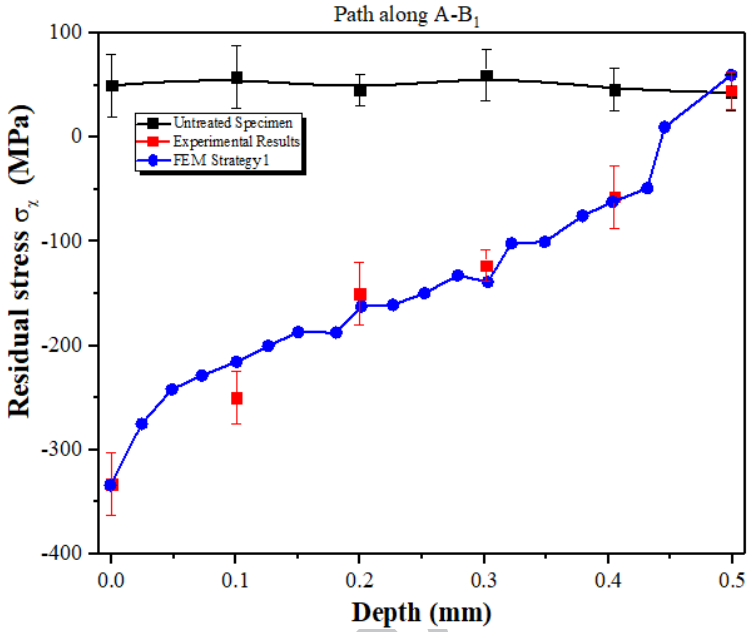

Fig. 6 Comparison between experimental and simulated results of strategy 1 along path A-B_1 of scanning path gradient at a depth of 0.5 mm.

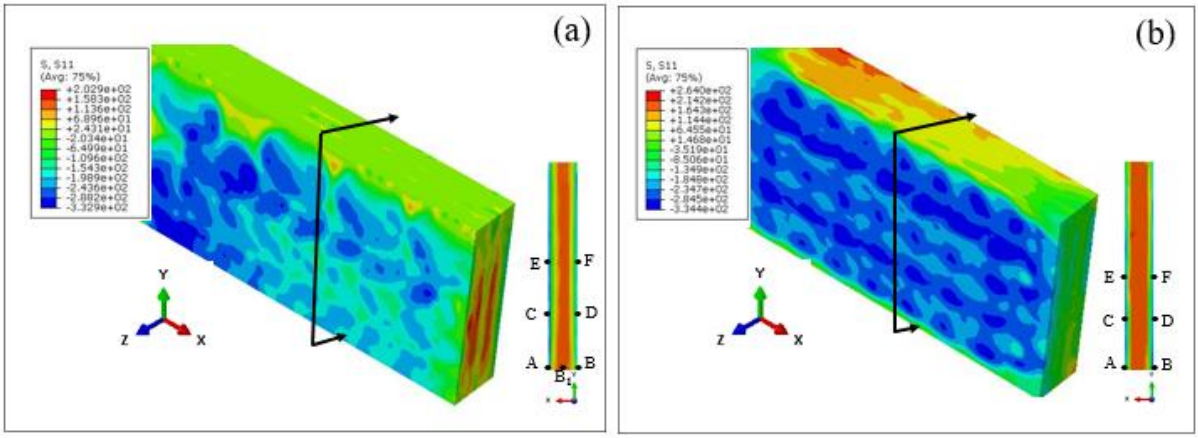

Fig. 7 Simulated residual stress results after (a) Strategy 1 and (b) Strategy 2.

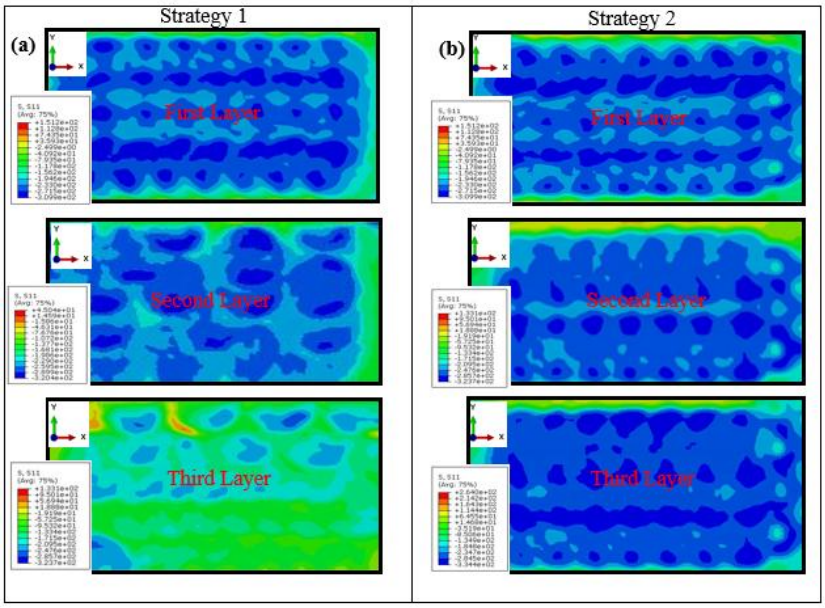

Fig. 8 2D simulation results after each scanning layer for; (a) Strategy 1 and (b) Strategy 2.

3.2 Residual stress comparison between strategy 1 and strategy 2

The points A-B, A-B_1, C-D and E-F have earlier been defined on the cross-section of the LSP treated specimen. Figs. 9-11 shows the residual stress distribution along the paths A-B, C-D and E-F at the various points for both strategy. The induced residual stress at the apex surface along the path A-B for strategy 1 was about -333 MPa and that for strategy 2 was about -334 MPa (see Table 5 and Fig. 9). The ultimate tensile stresses in the middle section of strategy 1 was 105 MPa, while that of strategy 2 was 110 MPa. There were no differences in strategy along path A-B for the induced residual stresses but, strategy 2 showed more tensile than strategy 1. The bottom surface of strategy 1 and strategy 2 for the residual stresses showed no differences with stress values of -250 MPa and -250 MPa, respectively. Tables 5-7 shows that the residual stress magnitude for the scanning path gradient along the paths A-B, C-D and E-F varying from each other. The residual stresses at the point along C-D for strategy 1 and strategy 2 at the apex surface was -305 MPa and -334 MPa, respectively (see Table 6 and Fig. 10). The middle section tensile residual stress along the path was 64 MPa and 100 MPa for strategy 1 and strategy 2, respectively. While the residual stresses at

the bottom surface for strategy 1 was -187 MPa and that of strategy 2 was -245 MPa. The change in residual stress magnitude was about 31%, meaning strategy 2 is more compressive than strategy 1. There were significant variations in the residual stress magnitude along the bottom surfaces of path A-B and that of C-D for both strategies. The analogy in both path A-B and C-D explains the edge material effect and how is affected by the assistance of the pulse sequence, besides the anisotropy generated through sequence overlapping [6]. Hence, the residual stress magnitude along the paths in both strategies was at maximum at the edges and decreases in depth towards the middle section where the tensile residual stress is comparatively high. Furthermore, the maximum residual stresses at the location along path E-F on the apex surface for strategy 1 and strategy 2 is -270 MPa and -334 MPa (see Table 7 and Fig. 11), respectively. The variations in residual stress at the apex surface for both strategy was 24%, making strategy 2 more compressive than strategy 1. The middle section tensile residual stress value was 71 MPa and 100 MPa, respectively. The introduction of tensile residual stresses have the tendency to fast track fatigue crack propagation, hence, influence the fatigue behaviour [41]. The bottom surfaces of both strategy values are -160 MPa and -260 MPa, respectively for strategy 1 and 2. There was significant variations in the residual stress magnitude between both strategies along the path. Thus, the difference in strategy at the bottom surface was 41%. The results demonstrate that the residual stress gradient of AA2024-T351 aluminum alloy specimen is dependent on the scanning path strategies employed.

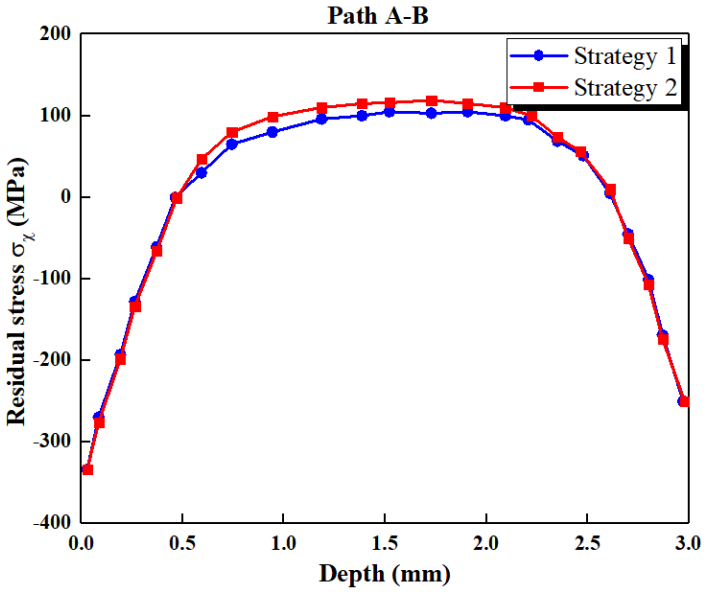

Fig. 9 Residual stress along path A-B: Comparison between strategy 1 and 2.

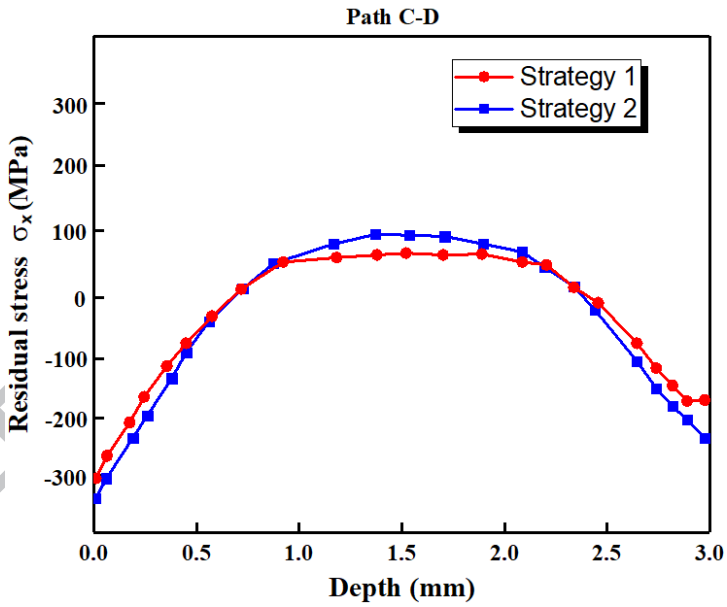

Fig. 10 Residual stress along path C-D: Comparison between strategies 1 and 2.

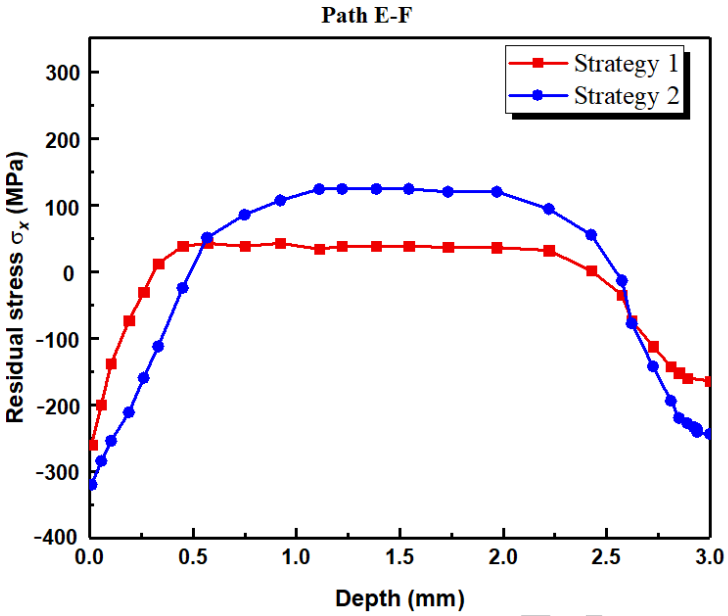

Fig. 11 Residual stresses along path E-F: Comparison between strategy 1 and 2.

Table 5 Residual stresses comparison between strategy 1 and 2 along path A-B.

Path	**A-B**	
Pulse sequence	**Strategy 1**	**Strategy 2**
Residual stress at apex surface (MPa)	-333	-334
Tensile stress at mid-section (MPa)	105	110
Residual stress at button surface (MPa)	-250	-250

Table 6 Residual stresses comparison between strategy 1 and 2 along path C-D.

Path	**C-D**	
Pulse sequence	**Strategy 1**	**Strategy 2**
Residual stress at apex surface (MPa)	-305	-334
Tensile stress at mid-section (MPa)	64	100
Residual stress at bottom surface (MPa)	-187	-245

Table 7 Residual stress comparison between strategy 1 and 2 along path E-F.

Path	**E-F**	
Pulse sequence	**Strategy 1**	**Strategy 2**
Residual stress at apex surface (MPa)	-270	-334
Tensile stress at mid-section (MPa)	71	100
Residual stress at bottom surface (MPa)	-160	-260

3.3 Fatigue life

A total of fifteen fatigue specimens were used, in which ten specimens were treated with the laser peening strategy 1 and 2, while five for the untreated specimen for comparative analysis. An improvement of fatigue life was noticed through strategy 2, although both strategies improved the fatigue lives of AA2024-T351 aluminum alloy specimen. The mean fatigue life and the fatigue life cycles results is shown in Tables 8 and 9 respectively, while Fig. 12 shows the fatigue properties of both untreated and LSP treated specimens. We observed that strategy 1 continued for approximately 35,292 cycles of fatigue failure and was about 69.3% improvement with reference to the untreated specimen with about 20,841 cycles of failure. While strategy 2 continued for about 40,321 cycles of fatigue failure which is also equivalent to an improvement of 93.5%. The differences in fatigue life after the LSP treatment is because of the scanning path gradient in strategy 1. The shockwaves generated high levels of plastic deformation at the surface and beneath the top surface of both strategies however, at the depth residual stress level, the number of impacts for strategy 1 at points C-D reduced from two shots to one shot at point E-F resulting into residual stress gradient along this path. The induced residual stress layer has the potential to retard the fatigue crack propagation in the laser-covered area. C. Correa et al. [6] studied the effect of swept direction on the fatigue life of 316L stainless steel alloy. Their results agree well with our results displayed in the present AA2024-T351 aluminum alloy, the authors stated that the improvement in fatigue life was noticed when the swept direction was parallel to the specimen longitudinal direction. In view of this, factors like tensile residual stress in the middle section (due to equilibrium of stress state) and residual stress introduced at the specimen edges [6], [42] are attributed to have high influence on the fatigue life. A. Salimianrizi [43] compared the zig-zag and spiral type swept directions in Al 6061-T6. The ultimate top surface hardness was achieved with the spiral swept direction. In addition, C.

Correa [17] suggested random type swept pattern, which accomplished considerable reduction in the residual stress anisotropy comparative to the zig-zag swept pattern.

Table 8 Mean fatigue life results for both untreated and LSP treated specimen.

Specimen number	Mean fatigue life of specimen	Percent fatigue life improvement	Std. Deviation
Untreated	20,841	-	1040.6
Strategy 1	35,292	69.3	522.3
Strategy 2	40,321	93.5	879.8

Table 9 Fatigue test results for both untreated and LSP treated specimens.

Specimen number	No. of cycles to failures (Untreated specimen)	No. of cycles to failures (Strategy 1)	No. of cycles to failures (Strategy 2)
1	19,839	36,155	41,267
2	22,435	35,251	39,126
3	19,989	34,890	40,001
4	20,855	35,300	41,110
5	21,087	34,864	40,101

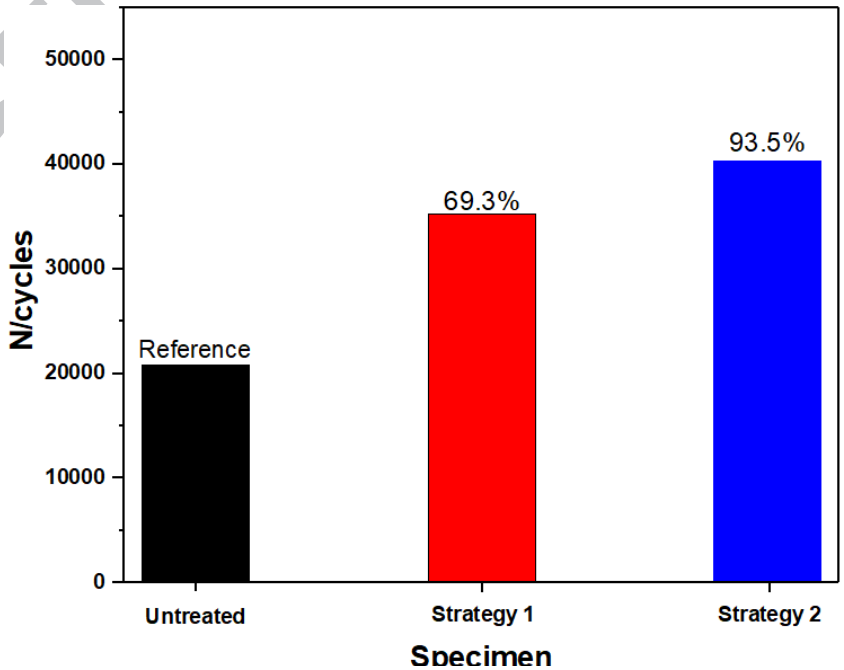

Fig. 12 Fatigue properties between untreated, strategy 1 and 2.

3.4 Fatigue fracture

Fig. 13 exhibit a typical fracture morphology of fatigue crack initiation sites for the untreated and the scanning gradient specimen. Fig. 13 (a) displays the SEM morphology of the untreated specimen, while Fig. 13 (b) displays the SEM morphology for the scanning gradient specimen. The crack initiation process of the untreated specimen in Fig. 13 (a) originated from the weakest location at the corner, where the stress was heavily concentrated[44]. Subsequent to fracture, we noticed an initial forming of crack initiation which increasingly enlarged, then fractured suddenly.

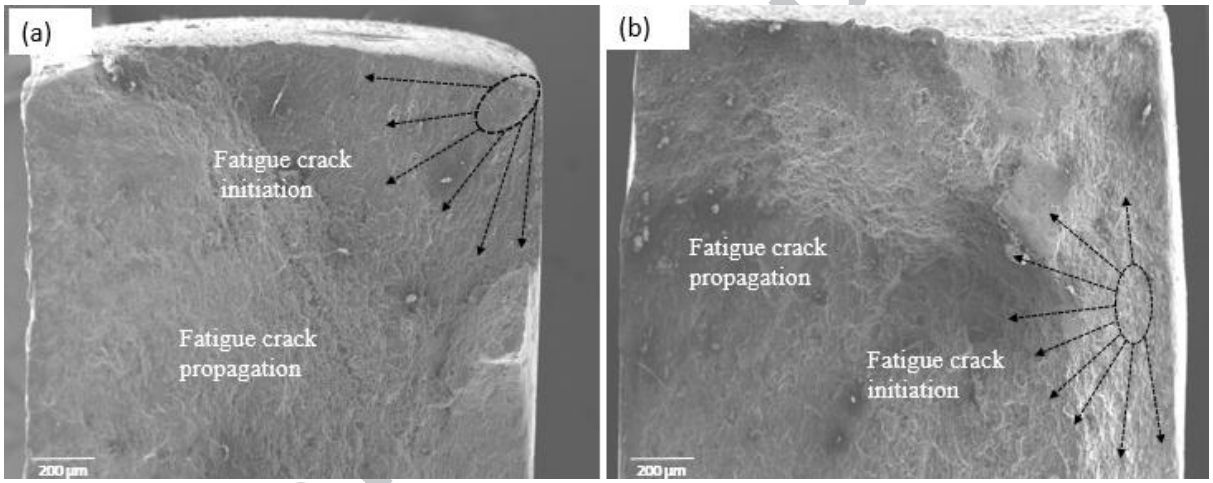

Fig. 13 Fatigue crack origin (a) untreated specimen (b) LSP specimen.

With the scanning gradient specimen, we observed again that the fatigue crack originated far away from the weakest location, thus originating from the subsurface layer. The difference in crack origin between the untreated and scanning gradient specimen is the result of the residual stress gradient generated by the LSP treatment on the surface of strategy 1, which retarded the fatigue crack nucleation and reduced the chances for the crack to initiate at the near surface. This results is also noticed by several authors including Ren et al. [42] on 7050-T7451 alloy, Vázquez Jiménez et al. [43] on 2205 DSS, Hongchao [44] on Ti17 titanium alloy, L. Zhang et al. [45] and X. Q. Zhang et al. [46] on aluminium alloy material. We also noticed from Fig. 14 (a) and (b) the presence of fatigue striations spacing which

looks like wave-pattern stripes [46] on both the untreated and scanning gradient specimen. Each of the fatigue striations spacing constitute applied cyclic load on the metallic material. The striations spacing are parallel to each other and arranged perpendicularly to the expansion direction of the fatigue crack. In the LSP treated specimen, the spacing between each striation spacing are small depicting steady fatigue crack growth rate whiles in the untreated specimen, show large spacing between them, hence depicting fast fatigue crack growth. The spacing between each fatigue striations is the distance of the fatigue crack growth per cycle [47],[49]. We also observed that the average striations spacing for the untreated specimen was about 0.70 ─ 0.85 μm/cycle and larger than the LSP treated specimen with about 0.20 ─ 0.35 μm/cycle.

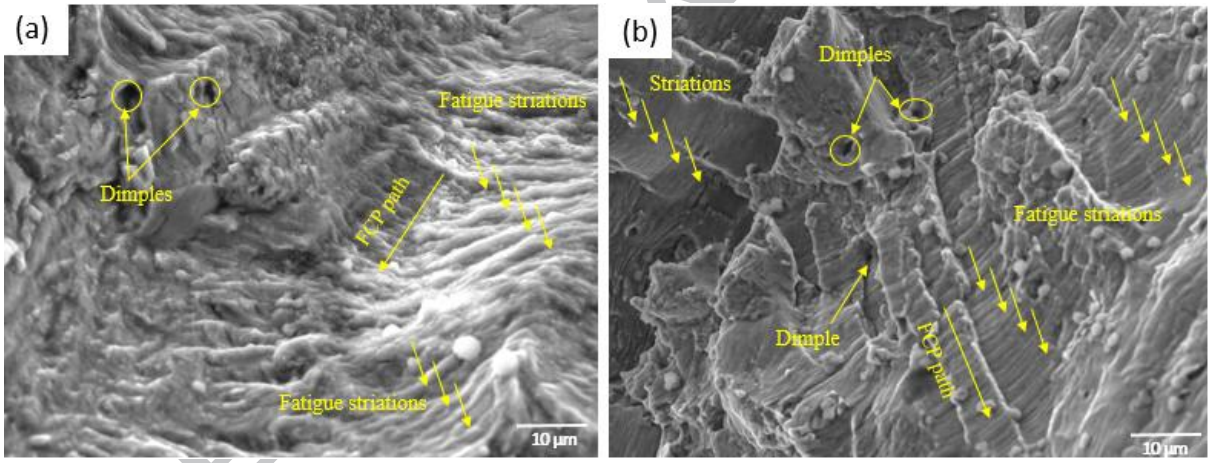

Fig. 14 Fatigue fracture morphology fatigue striation spacing (a) Untreated (b) LSP specimen.

We observed in Fig. 15 (a) and (b) the presence of dimples on the rapidly increasing fatigue crack. With the increase in strain, the micro cavities continue to build-up resulting in isometric dimples on the fractured near surfaces, with inclusions located at the bottom of the dimples [44]. The dimples in the fatigue fracture in Fig. 15(a) of the untreated specimens are much smaller than the dimples in the fatigue fracture in Fig. 15(b) of the scanning gradient specimens. The untreated specimens showed equiaxed dimples, and the scanning gradient specimens exhibited elongated dimples after the fatigue fracture. It is revealed that elongated

dimples show a ductile rupture [50 - 52]. It is also reported by Zhang et al. that the dimples could be influenced by the properties of the metallic material like deformation capacity and work hardening exponent [53].

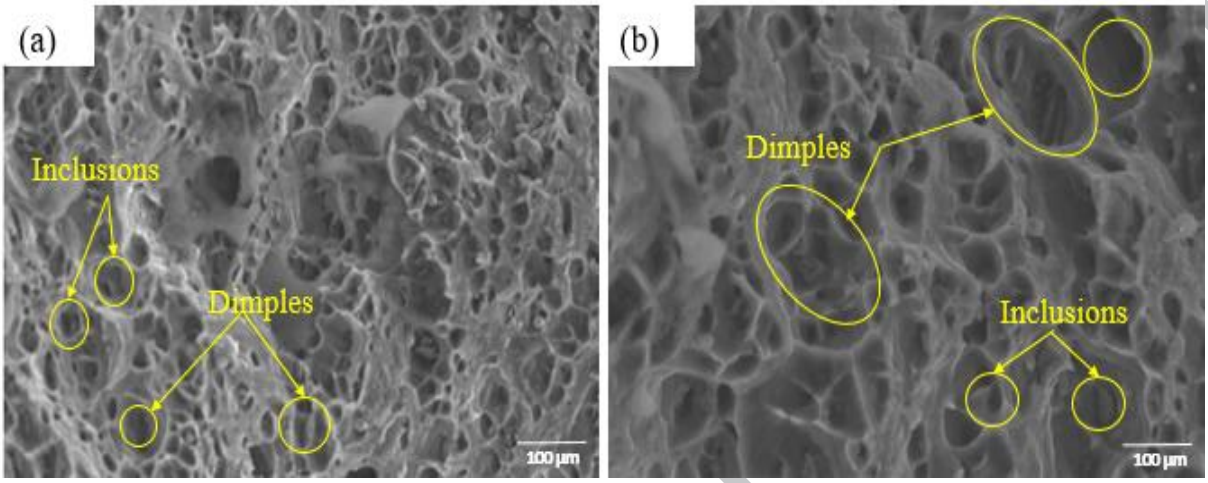

Fig. 15 Final fatigue morphologies of AA2024-T351 aluminum (a) Untreated and (b) LSP specimen.

4. Conclusion

In summary, this paper presents the effects of scanning path gradient on the residual stress distribution and fatigue life by LSP on AA2024-T351 aluminum alloy. The FE method was used to predict the residual stress distribution induced by LSP on the double-sided specimen. The authors conclude on the following points.

(1) Results of the FE simulation revealed that the residual stress distribution was advertently influenced by the scanning path strategy employed. The prediction of the residual stress by the FE simulation correlates well with the experimental results. Though, LSP induces beneficial residual stresses, it also introduced unsuitable tensile residual stresses in the mid-thickness of the double-sided LSP treated aluminum alloy specimen.

(2) Both strategy 1 and strategy 2 increased the fatigue life of the aluminum alloy specimen. Under strategy 1, an increase in fatigue life of 35,292 × 10^5 cycles was observed, while strategy 2 also experienced fatigue life increase of 40,321 × 10^5 cycles. Both strategy 1 and strategy 2 experienced 69.3% and 93.5% percent improvement in fatigue life respectively, compared to the untreated specimen.

(3) The increase in fatigue life of the aluminum alloy specimen depended on the magnitude and depth of the residual stress gradient. The induced residual stresses on the specimen top and bottom surfaces after LSP retarded the growth of the fatigue crack initiation and propagation sequentially.

Acknowledgement

The authors are very much grateful to the Natural Science Foundation of Jiangsu Province (Grant No. BK20160014), the project is supported by the National Natural Science Foundation of China (Grant No. 51479082), the ‘‘333 Project’’ of Jiangsu Province (Grant No. BRA2017389), and the 2015 Innovation & Entrepreneurship Project of Jiangsu Province.

References

[1] X. C. Zhang, Y. K. Zhang, J. Z. Lu, *et al.*, Improvement of fatigue life of Ti – 6Al – 4V alloy by laser shock peening, *Material Science Engineering A*, 527 (15) (2010) 3411–3415.

[2] O. Hatamleh, P. M. Singh, H. Garmestani, Corrosion susceptibility of peened friction stir welded 7075 aluminum alloy joints, *Corrosion Science*, 51 (2009) 135–143.

[3] U. Sánchez-Santana, C. Rubio-Gonzalez, G. Gomez-Rosas, *et al.*. Wear and friction of 6061-T6 aluminum alloy treated by laser shock processing, *Wear*, 260 (7–8) (2006) 847–854.

[4] Braisted William, Robert Brockman, Finite Element Simulation of Laser Shock Peening, *International Journal of Fatigue*, 21(7) (1999) 719–724.

[5] Hu Yongxiang, Zhenqiang Yao, Jun Hu, 3-D FEM simulation of laser shock processing, *Surface Coatings Technology*, 201(3–4) (2006) 1426–1435.

[6] C. Correa, L. Ruiz de Lara, M. Díaz, A. Gil-Santos, J. A. Porro, J. L. Ocaña, Effect of advancing direction on fatigue life of 316L stainless steel specimens treated by double-sided laser shock peening, *International Journal of Fatigue*, 79 (1–9) 2015.

[7] Ding Kan, Lin Ye, Laser Shock Peening Performance and Process Simulation, *Woodhead Publishing, Cambridge, England*, 2006.

[8] B. K. Pant, A. H. V. Pavan, R. V. Prakash, M. Kamaraj, Effect of laser peening and shot peening on fatigue striations during FCGR study of Ti-6Al-4v, *International Journal of Fatigue*, 93 (2016) 38–50.

[9] P. Peyre, R. Fabbaro, Laser shock processing: a review of the physics and applications, *Opt. Quantum Electron.*, 27 (1995) 1213–1229.

[10] C. A. Rodopoulos, A. T. Kermanidis, E. Statnikov, *et al.*, The Effect of Surface Engineering Treatments on the Fatigue Behavior of 2024-T351 Aluminum Alloy, *J. Mater. Eng. Perform.*16 (1) (2007) 30–34.

[11] C. Ye, S. Suslov, B. J. Kim, *et al.*, Fatigue performance improvement in AISI 4140 steel by dynamic strain aging and dynamic precipitation during warm laser shock peening, *Acta Mater.*, 59 (3) (2011) 1014–1025.

[12] Y. Sano, M. Obata, T. kubo *et al.*, Retardation of crack initiation and growth in

austenitic stainless steels by laser peening without protective coating, *Mater. Sci. Eng. A*, 417 (1–2) (2006) 334–340.

[13] X. Nie, W. He, L. Zhou, *et al.*, Experiment investigation of laser shock peening on TC6 titanium alloy to improve high cycle fatigue performance, *Mater. Sci. Eng. A*, 594, (2014) 161–167.

[14] Z. Zhou, S. G. Amrinder, D. Qian *et al.*, A finite element study of thermal relaxation of residual stress in laser shock peened IN718 superalloy, *Int. J. Impact Eng.*, 38 (7) (2011) 590–596.

[15] J. H. Kim, J. W. Lee, Effects of simulation parameters on residual stresses in 3D Finite Element laser shock peening analysis, *Glob. Journal of Res. in Eng.*, 13 (9) (2013).

[16] K. Ding, Three-dimensional dynamic finite element analysis of multiple laser shock peening processes, *Surf. Eng.*, 19 (5) (2003) 351–358.

[17] C. Correa, D. Peral, J. A. Porro, *et al.*, Random-type scanning patterns in laser shock peening without absorbing coating in 2024-T351 Al alloy: A solution to reduce residual stress anisotropy, *Opt. Laser Technol.*, 73 (2015) 179–187.

[18] C. Correa, L. Ruiz de Lara, M. Díaz, *et al*. Influence of pulse sequence and edge material effect on fatigue life of Al2024-T351 specimens treated by laser shock processing, *Int. J. Fatigue*, 70 (2015) 196–204.

[19] P. Peyre, I. Chaieb, C. Braham, FEM calculation of residual stresses induced by laser shock processing in stainless steels, *Model. Simul. Mater. Sci. Eng.*, 15 (3) (2007) 205.

[20] H. K. Amarchinta, R. V Grandhi, K. Langer, *et al.*, Material model validation for laser shock peening process simulation, *Model. Simul. Mater. Sci. Eng*, 17 (15) (2009).

[21] C. Su, J. Zhou, X. Meng, S. Huang, Improvement in fatigue performance of aluminium alloy welded joints by laser shock peening in a dynamic strain aging temperature regime, *Materials (Basel).*, 9 (10) (2016) 799.

[22] P. Peyre, C. Braham, J. Lédion, L. Berthe, *et al.*, Corrosion reactivity of laser-peened steel surfaces, *J. Mater. Eng. Perform.*, 9 (6) (2000) 656–662.

[23] L. Petan, J. L. Ocaña, J. Grum, Influence of laser shock peening pulse density and spot size on the surface integrity of X2NiCoMo18-9-5 maraging steel, *Surf. Coatings Technol.*, 307 (2016) 262–270.

[24] S. Kalainathan, S. Prabhakaran, Recent development and future perspectives of low energy laser shock peening, *Opt. Laser Technol.*, 81 (2016) 137–144.

[25] T. A. DeWald, J. E. Rankin, M. R. Hill, *et al*., Assessment of tensile residual stress mitigation in alloy 22 welds due to laser peening, *J. of Eng. Mater. and Technol.*, 126 (4) (2004) 465–473.

[26] Y. Tan, G. Wu, J-M. Yang, *et al.*, Laser shock peening on fatigue crack growth behaviour of aluminium alloy, *Fatigue & Fract. of Eng. Mater. & Struct.*, 27 (8) (2004) 649–656.

[27] S. Adu-Gyamfi, X. D. Ren, E. A. Larson, *et al.*, The effects of laser shock peening scanning patterns on residual stress distribution and fatigue life of AA2024 aluminium alloy, *Opt. Laser Technol.*, 108 (2018) 177–185.

[28] K. Ding, L. Ye, Simulation of multiple laser shock peening of a 35CD4 steel alloy, *J. of Mater. Process. Technol.*, 178 (1–3) (2006) 162–169.

[29] A. Gariépy, F. Bridier, M. Hoseini, *et al.*, Experimental and numerical investigation of material heterogeneity in shot peened aluminium alloy AA2024-T351. *Surf. Coat. Technol*. 219 (2013) 15–30.

[30] Hombergsmeier E, Holzinger V, Heckenberger UC. Fatigue crack retardation in LSP and SP treated aluminium specimens. *Adv Mater Res* (2014) 891–892:986–91.

[31] Y. Cao, X. Xie, J. Antonaglia *et al.*, Laser shock peening on zr-based bulk metallic glass and its effect on plasticity: Experiment and modeling. *Sci. Rep.*, 5 (2015) 10789.

[32] P. Peyre, R. Fabbro, P. Merrien, *et al.*, Laser shock processing of aluminium alloys. Application to high cycle fatigue behaviour, *Mater. Sci. Eng. A*, 210 (1–2) (1996) 102–113.
[33] J. N. Johnson, R. W. Rohde, Dynamic deformation twinning in shock ‐ loaded iron, *J. Appl. Phys.*, 42 (11) (1971) 4171–4182.
[34] Ling X., W. Peng, G. Ma, Influence of laser peening parameters on residual stress field of 304 stainless steel, *J. Press. Vessel Technol.*, 130 (2) (2008) 021201.
[35] C. Yang, P. Damian, Q. Liu, *et al.*, Geometrical effects on residual stresses in 7050-T7451 aluminum alloy rods subject to laser shock peening, *J. Mater. Process. Technol.*, 1 (2008) 303–309.
[36] R. Fabbro, J. Fournier, P. Ballard, *et al.*, Physical study of laser- produced plasma in confined geometry, *J. Appl. Phys.*, 68 (1990) 775–784.
[37] J. Fournier, P. Ballard, P. Merrien, *et al.*, Mechanical effects induced by shock waves generated by high energy laser pulses, *J. Phys. III*, 1(9) (1991) 1467–1480.
[38] J. Zhao, Y. Dong, C. Ye, Laser shock peening induced residual stresses and the effect on crack propagation behavior, *Int. J. Fatigue*, 100 (2017) 407–417.
[39] S. Bhamare, G. Ramakrishnan, S. R. Mannava, *et al.*,Simulation-based optimization of laser shock peening process for improved bending fatigue life of Ti–6Al–2Sn–4Zr–2Mo alloy, *Surf. Coatings Technol.*, 232 (2013) 464–474.
[40] A. Salimianrizi, E. Foroozmehr, M. Badrossamay, *et al.*, Effect of Laser Shock Peening on surface properties and residual stress of Al6061-T6, *Opt. Lasers Eng.*, 77 (2016) 112–117.
[41] X. Zhang, L. Chen, X. Yu, *et al.*, Effect of laser shock processing on fatigue life of fastener hole, *Trans. Nonferrous Met. Soc. China*, 24 (4) (2014) 969–974.
[42] X. D. Ren, Q. B. Zhan, H. M. Yang, *et al.*, The effects of residual stress on fatigue behavior and crack propagation from laser shock processing-worked hole, *Mater. Des.*, 44 (2013) 149–154.
[43] C. A. Vázquez Jiménez, G. Gómez Rosas, C. Rubio González, *et al.*, Effect of laser shock processing on fatigue life of 2205 duplex stainless steel notched specimens, *Opt. Laser Technol.*, 97 (2017) 308–315.
[44] Q. Hongchao, Experimental investigation of laser peening on Ti17 titanium alloy for rotor blade applications, *Appl. Surf. Sci.*, 351 (2015) 524–530.
[45] L. Zhang, J. Z. Lu, Y. K. Zhang, *et al.*, Effects of different shocked paths on fatigue property of 7050-T7451 aluminum alloy during two-sided laser shock processing, *Mater. Des.*, 32 (2) (2011) 480–486.
[46] X. Q. Zhang, H. Li, X. L. Yu, *et al.*, Investigation on effect of laser shock processing on fatigue crack initiation and its growth in aluminum alloy plate, *Mater. & Des.*, 65 (2015) 425–431.
[47] A. Chahardehi, F. P. Brennan, A. Steuwer, The effect of residual stresses arising from laser shock peening on fatigue crack growth, *Eng. Fract. Mech.*, 77(11) (2010) 2033–2039.
[49] S. Huang, J. Z. Zhou, J. Sheng, *et al.*, Effects of laser peening with different coverage areas on fatigue crack growth properties of 6061-T6 aluminum alloy, *Int. J. Fatigue*, 47 (2013) 292–299.
[50] A. Ahmadi, MR. Toroghinejad, A. Najafizadeh. Evaluation of microstructure and mechanical properties of Al/Al2O3/SiC hybrid composite fabricated by accumulative roll bonding process. *Mater. & Des.*, 53 (2014) 13–9.
[51] Z. Hamouche-Hadjem, T. Auger, I. Guillot, *et al.*, Susceptibility to LME of 316L and T91 steels by LBE :effect of strain rate. *J. Nucl. Mater.*, 376 (2008) 317–21.
[52] T. S. Srivatsan, S. Vasudevan, L. Park. The tensile deformation and fracture behavior

of friction stir welded aluminum alloy 2024. *Mater. Sci. Eng. A* 466 (2007) 235–45.

[53] L. Zhang, K. Y. Luo, J. Z. Lu *et al.*, Effects of laser shock processing with different shocked paths on mechanical properties of laser welded ANSI 304 stainless steel joint. *Mater. Sci. Eng. A*.528 (2011) 4652–7.

Highlights

- Two divergent strategies was peened on AA2024-T351 aluminum alloy.
- Increased in fatigue life for both strategy was observed after LSP.
- Residual stress fields and fatigue life were influenced by the scanning gradient.
- A good correlation was observed between the FE and the experimental results.

Graphical Abstract